

**Physicochemical controls on bismuth mineralization, Serifos  
Island, Cyclades, Greece.**

MICHALIS FITROS<sup>1</sup>, STYLIANOS F. TOMBROS<sup>1</sup>,

ANTHONY E. WILLIAMS-JONES<sup>2</sup>, BASILIOS TSIKOURAS<sup>1,3</sup>,

ELENI KOUTSOPOULOU<sup>1</sup>, KONSTANTIN HATZIPANAGIOTOU<sup>1</sup>

<sup>1</sup>Department of Geology, Section of Earth Materials, University of Patras, Rion, 26500,  
Patras, Greece

<sup>2</sup>Department of Earth and Planetary Sciences, 3450 University Street, Montreal, Quebec  
H3A 2A7, Canada

<sup>3</sup>Universiti Brunei Darussalam, Faculty of Science, Physical and Geological Sciences,  
Jalan Tungku Link, BE1410 Gadong, Bandar Seri Begawan, Brunei Darussalam

**Abstract:** The 11.6 to 9.5 Ma Serifos pluton intruded schists and marbles of the  
Cycladic Blueschist unit, causing thermal metamorphism, the development of magnetite  
Ca-exo- and endo-skarns and the formation of low-temperature vein and carbonate-  
replacement ores. Potentially, the most important ores occur in the Moutoulas prospect

where the mineralization in retrograde skarn and quartz veins culminated with the deposition of native bismuth. A combination of fluid inclusion microthermometry and isotope geothermometry suggests that the Moutoulas mineralization formed at a hydrostatic pressure of ~100 bars, from moderate-to-low temperature (~190–250 °C), and low-salinity (1.3–5.6 wt% NaCl equivalent) fluids. The calculated  $\delta^{34}\text{S}_{\text{H}_2\text{S}}$  compositions are consistent with the ore fluids having been derived from the Serifos pluton. Bismuth mineralization is interpreted to have occurred as a result of wall-rock interaction and mixing of a Bi-bearing ore fluid with meteoric waters. Native bismuth and bismuthinite deposited at ~200 °C, near neutral pH (6.5), low  $f\text{S}_2$  (< -16.5), and low  $f\text{O}_2$  (< -44). Supergene alteration in Serifos led to the oxidation of native bismuth to bismite and bismutite.

**Keywords:** Native bismuth, retrograde skarn, supergene alteration, Moutoulas, Serifos.

## Introduction

Knowledge of the aqueous geochemistry of bismuth, in particular, the physicochemical controls of its transportation and deposition is still incomplete. Experimental and theoretical studies (e.g., Skirrow et al. 2002; Tooth et al. 2008; Mavrogenes et al. 2010; Henley et al. 2012; Etschmann et al. 2016) suggest that Bi can be mobile either in vapors at high temperature or in the liquid as complexes of  $\text{Bi}^{3+}$  ions with hydroxyl and chloride ions, e.g.,  $\text{Bi}_n(\text{OH})_m^{+x}$  ( $x=1$  and  $2$ ,  $n=1, 6$ , and  $9$  and  $m=12, 20$ , and  $21$ ),  $\text{Bi}(\text{OH})_3$ ,  $\text{BiCl}_n^{+x}$  ( $x=1$  and  $2$ ,  $n=1$  and  $2$ ),  $\text{BiCl}_n^{-x}$  ( $x=1, 2$ , and  $3$ ,  $n=4, 5$  and  $6$ ) and  $\text{BiCl}_3$ .

Occurrences of native bismuth in Greece are found mainly in the Servomacedonian, Rhodope and Atticocycladic massifs in Cu-Mo porphyries, skarns, carbonate replacement deposits and related vein stockworks, volcanic-hosted epithermal deposits and in shear-zone deposits (Voudouris et al., 2007 and references therein; Cook et al., 2009). In these deposits, the native bismuth is intergrown with bismuthinite, galena, Bi-sulfosalts (gustavite, lillianite, aikinite and cosalite), Bi-tellurides and electrum or occurs as inclusions in galena (Voudouris et al. 2007). Supergene alteration of native bismuth led to the formation of bismite and bismutite. This study focuses on the Moutoulas deposit, an unexploited prospect, on Serifos Island, where native bismuth precipitated in clear quartz veins. In it, we investigate the physicochemical controls on the precipitation of native bismuth as a retrograde skarn mineral and its subsequent supergene alteration. We introduce a new approach for the calculation of  $\text{Bi}(\text{OH})^{2+}$  contours over temperature with the aim to predict the favorable conditions in which native bismuth precipitates. It is proposed that bismuth was transported as complexes involving hydroxyl and bicarbonate ions, e.g.,  $\text{Bi}(\text{OH})_x^{3-x}(\text{HCO}_3)_y^{3-y}$  and that it deposited as native bismuth during mixing of the ore fluid with meteoric water.

### **Geological Setting**

Serifos Island is part of the Attico-Cycladic massif of Greece, which includes three nappes: the lower Cycladic Basement Unit consisting of gneisses of Variscian ages (CB), the Cycladic Blueschist Unit (CBU), and the Upper Cycladic Unit (UCU) (Rabillard et al. 2015). The CB in Serifos comprises alternating hornblende- biotite and quartzo-feldspathic

gneisses, intercalated with quartzites and marbles, and the CBU, amphibolites intercalated with gneisses and greenschists containing thinly bedded dolomitic marbles. The latter unit represents a metamorphosed volcanosedimentary sequence developed along a Mesozoic continental margin. At least two Tertiary metamorphic events affected the CBU. The first event occurred between 53 and 40 Ma and was characterized by eclogite to blueschist facies conditions ( $T = 450\text{--}500\text{ }^{\circ}\text{C}$ ,  $P = 1.5 \pm 0.3\text{ GPa}$ , Brichau et al. 2010). This event was followed by a greenschist to amphibolite facies event ( $T = 670\text{--}700\text{ }^{\circ}\text{C}$  and  $P = 0.4\text{--}0.7\text{ GPa}$ , Xypolias et al. 2012) that occurred between  $\sim 25$  and  $\sim 12$  Ma (Bolhar et al. 2010). The UCU comprises an ophiolite nappe that was obducted in the Late Jurassic, and is overlain by unmetamorphosed sedimentary rocks (Bröcker and Franz 2005; Rabillard et al. 2015). The following lithotypes of UCU occur in Serifos (Fig. 1): calcitic marbles, ankerite-dolomite-talc-goethite carbonate-replacement orebodies, meta-basites, and serpentinites (Grasemann and Petrakakis 2007; Petrakakis et al. 2007). The lower Megalo Livadi detachment (ML) separates the CB from the CBU, and the upper Kavos Kiklopas detachment (KK) separates the CBU from the UCU (Grasemann et al. 2012; Ducoux et al. 2017; Fig. 1). The Serifos pluton was emplaced at  $\sim 11.6$  to  $9.5$  Ma in the CB and CBU rocks along the NE-SW trending ML detachment, creating a contact metamorphic aureole,  $0.5$  to  $1$  km in width (Fig. 1, Rabillard et al. 2015). I-type, hornblende-biotite granodiorite with subordinate tonalite intruded at its center, and granodiorite to S-type hornblende-biotite-allanite-zinnwaldite granite at its margins (Stouraiti and Mitropoulos 1999; Grasemann and Petrakakis 2007; Seymour et al. 2009). The pluton crystallized at a temperature of  $\sim 700$  to  $750\text{ }^{\circ}\text{C}$  and was emplaced at a pressure of  $0.15$  to  $0.35\text{ GPa}$

(Seymour et al. 2009). Granodioritic to granitic apophyses, zoned pegmatites, aplites, and dacitic dikes intruded the CBU rocks along NW-SE trending, counterclockwise reverse faults (Fig. 1). Their ages range from 8.2 to 8.7 Ma (Altherr et al. 1982), and they formed at  $T = 650\text{ }^{\circ}\text{C}$  and  $P = 0.1\text{--}0.2\text{ GPa}$  (Stouraiti and Mitropoulos 1999; Seymour et al. 2009). Pyroxene-garnet exoskarns occur in the CBU marbles and garnet- and pyroxene-garnet endoskarns in the pluton (Ducoux et al. 2017; Fig. 1). The exoskarns comprise diopside-hedenbergite, andradite, wollastonite, and magnetite and minor suanite ( $\text{Mg}_2\text{B}_2\text{O}_5$ ) (Salemink 1985; Seymour et al. 2009; Fig. 1). Formation of ore minerals in the Serifos exoskarn began with the deposition of high-temperature magnetite at the contact of the pluton with the CBU (Fig. 1). Subsequent retrograde skarn formation at Moutoulas (~1 km from the pluton contact, Fig. 1) resulted in the precipitation of pyrite, sphalerite, chalcopyrite, galena, and native bismuth. The mineralization takes the form of lenses up to  $0.5 \times 40 \times 25\text{ m}$  in size that mainly replaced the CBU marbles, and it is interpreted to represent an early carbonate replacement event (Seymour et al. 2009). Four major syntaxial quartz veins trending NNW-SSE (up to 100 m long and 0.5 m wide) cross-cut the CBU schists and marbles and are surrounded by alteration halos comprising an inner silica + sericite + pyrite  $\pm$  calcite zone (replacing orthoclase and albite of the CBU schists) and an outer epidote  $\pm$  chlorite, barite, pyrite, and galena zone (Fig. 2a). The magnetite and sulfide ores underwent later supergene oxidation.

## **Analytical Methods**

The ore minerals were identified using a combination of reflected light microscopy and X-ray diffraction (XRD) on a D8 Advance diffractometer (Bruker AXS) equipped with a LynxEye strip silicon detector. The X-ray diffractometer employed Ni-filtered CuK $\alpha$  radiation, a voltage of 35 kV, a 35 mA current, and 0.298° divergence and antiscatter slits. Random powder mounts of samples were scanned from 2 to 70° 2 $\theta$  with a scanning step of 0.015° 2 $\theta$ , and with 18.7 s count time per step, at the Research Laboratory of Minerals and Rocks, Department of Geology, University of Patras, Greece. Data were evaluated with the DIFFRACplus EVA v12.0 software and were compared with the PDF-2 database (ICDD, Newtown Square, Pennsylvania, U.S.A.).

Ore mineral compositions were determined using a JEOL 8900 Superprobe equipped with energy- and wavelength-dispersive spectrometers (EDS and WDS, respectively) and an xClent system for parts per million level resolution, at the Microprobe Center of the Department of Earth and Planetary Sciences Department, McGill University. The operating conditions were an acceleration voltage of 15kV, a beam current of 10 nA, and counting time of 20 s for all elements except Ag, As, and Te for which the counting times were 100 and 50 s, respectively. The standards used were natural chalcopyrite, tetrahedrite, tennantite, stibnite, pyrite, sphalerite, and galena, synthetic CoNiAs, SnO<sub>2</sub>, and CdTe, and the native metals Ag, Au, and Se. Minimum detection limits were 200 ppm for S; 300 ppm for Mn, Cd, and Se; 400 ppm for Ag, Te, and Au; 500 ppm for Zn, Fe, and Co; 600 ppm for Sb and Bi; 700 ppm for Cu and As; and 2000 ppm for Pb.

Microthermometric measurements were performed on two doubly polished 50–100  $\mu\text{m}$  thick wafers in which clear quartz was in intergrowth with pyrite, sphalerite, or native bismuth. The Linkam MDSG600 heating-freezing stage coupled to a ZEISS microscope in the Department of Earth Sciences and Resources, China University of Geosciences, Beijing, China, was used for this purpose. Temperatures were measured with an alumel-chromel thermocouple and the readings were calibrated with synthetic inclusions at  $-56.6\text{ }^{\circ}\text{C}$  (triple point of  $\text{CO}_2$ ),  $0.0\text{ }^{\circ}\text{C}$  (melting point of ice), and  $+374.1\text{ }^{\circ}\text{C}$  (critical point of  $\text{H}_2\text{O}$ ). Freezing-heating rates were maintained between  $0.2$  and  $5\text{ }^{\circ}\text{C}/\text{min}$  and measurements were accurate to  $\pm 0.1\text{ }^{\circ}\text{C}$ . Microthermometric data were reduced using the FLINCOR software (Brown 1989).

A subset of the fluid inclusions was analyzed using Laser Raman spectroscopy. This was done prior to microthermometric analysis in the Beijing Research Institute of Uranium Geology, China. The inclusions were analyzed for the common gases, mono- and poly-atomic ions and molecules via gas and ion chromatography. Gaseous composition was measured via a LabRAM HR800 Raman spectroscopic microscope, with a laser beam spot size of  $\sim 1\text{ }\mu\text{m}$ . The instrument recorded peaks ranging from  $100\text{--}4000\text{ cm}^{-1}$  with a spectral resolution of  $1\text{--}2\text{ cm}^{-1}$ , and their peaks identified using the reference catalog of Frezzotti et al. (2012). The relative concentrations (in mol%) of these species were calculated from the equations of Frezzotti et al. (2012) and the cross-sectional scattering coefficients of Dhamelincourt et al. (1979), using the LabSpec software. Liquid composition analysis was carried out with a Shimadzu HIC-SP Super ion chromatograph on double distilled water

leaches using the method of Yardley et al. (1993). The analytical precision for all gases analyzed was  $\pm 1\%$ , whereas for the cations and anions  $\pm 0.1$  ppm.

Fifteen sulfide mineral samples were analyzed for their sulfur isotope compositions. Only crystals of a given sulfide in textural equilibrium with contiguous crystals were selected for analysis to be used for geothermometry. These crystals were handpicked after examination under a binocular microscope to ensure textural equilibrium and a purity of  $\geq 98\%$ . Isotopic compositions of sulfur were analyzed with a VGMM602E double collector mass spectrometer at the Chinese Academy of Geological Sciences (CAGS), Beijing, China. Sulfur from vein pyrite, chalcopyrite, sphalerite, greenockite, and galena was released using the method of Fritz et al. (1974). The sulfur isotopic ratios are reported in standard  $\delta$  notation per mil relative to V-CDT. Analytical precision was better than  $\pm 0.2\%$  for  $\delta^{34}\text{S}$ . We used the AlphaDelta software (Beaudoin and Therrien 2009) to compute the isotopic fractionation factors and temperatures for mineral pairs in isotopic equilibrium. In addition, we analyzed pyrite and galena for their lead isotope compositions. Lead isotopic compositions were determined using an England Nu Plasma High Resolution type MC-ICP-MS with standard NBS-981, following the method of Yuan et al. (2013). Long-term repeated measurements of lead isotopic ratios of standard NBS981 yielded  $^{206}\text{Pb}/^{204}\text{Pb} = 16.9397 \pm 0.001$  and  $^{207}\text{Pb}/^{204}\text{Pb} = 15.4974 \pm 0.001$  (all errors are reported at  $\pm 2\sigma$ ).

## **The Moutoulas Mineralization**



Examination of the quartz veins reveals four distinct paragenetic stages of hydrothermal mineralization that can be recognized on the basis of mineralogical and textural relations (Fig. 2b, Table 1). The stage I assemblage occupies the margins of the veins and is characterized by massive, brecciated aggregates of subhedral pyrite with intergrowths of minor arsenopyrite, sphalerite ( $X_{\text{FeS}} = 20.7\text{--}25.8$ ), chalcopyrite, and pyrrhotite (Figs. 2b, 3a, and 3b). Pyrite crystals incorporate appreciable amounts of Bi as submicroscopic grains of bismuthinite (Supplemental Table 1). Stage II is represented by Bi- and Te-rich tetrahedrite-tennantite solid solutions ( $X_{\text{As}} = 1.9$  to  $2.3$ ) and sphalerite ( $X_{\text{FeS}} = 13.8\text{--}18.7$ ) filling brecciated pyrite (Fig. 3c, Supplemental Table 1), as well as minor greenockite and gersdorffite. Frequently, tetrahedrite-tennantite is observed to have replaced pyrite from stage I (Fig. 3c). Stage III occurs toward the vein center and consists of Bi-bearing galena, which intergrows with fluorite and calcite and replaces stage I and II minerals (Fig. 3d, Supplemental Table 1).

The stage IV assemblage develops in three sub-stages, as disseminations replacing stage III galena in the central parts of the veins (Figs. 2c, 3e, and 3f; Table 1; Supplemental Table 1). Calcite, fluorite, and barite also represent this stage. The early sub-stage includes euhedral acicular bismuthinite (Fig. 3e). The middle sub-stage comprises tellurides, including tetradymite, hessite, and melonite, and is succeeded by the late sub-stage that is dominated by native bismuth (Figs. 3e and 3f). In places, native bismuth replaced bismuthinite (Fig. 3f). During subsequent supergene alteration, mixtures of beyerite, bismutite, and bismite replaced native bismuth (Figs. 2c, 3e, 3f, and 4; Supplemental

Table 1). Covellite, cerussite, anglesite, chalcocite, goethite, azurite, and malachite also are products of this supergene stage (Table 1, data not shown).

### **Fluid Inclusion Studies**

Fluid inclusion data were obtained for two undeformed samples containing clear quartz and sphalerite; the data are for stages I and IV. The analyzed fluid inclusions assemblages (FIAs) occur individually or as small randomly oriented clusters (4–10  $\mu\text{m}$  in diameter). These inclusions are considered as primary in origin following the criteria of Roedder (1984). Their shapes include elliptical, negative crystal, and irregular forms without signs of necking down (Figs. 4a and 4b). Inclusions were considered to be secondary if they occur in planar arrays interpreted to be healed fractures that do not terminate at growth zones or grain boundaries (Figs. 4a and 4b).

At room temperature, only one type of fluid inclusions was recognized, namely L-V inclusions, consisting of aqueous liquid and vapor, with the liquid being dominant (accounting for ~90 vol% of the total fluid inclusion volume; Supplemental Table 2, Fig. 4b). Neither daughter crystals, trapped solids nor clathrates were observed. The temperature of initial melting of ice ranged from  $-23.8$  to  $-21.1$   $^{\circ}\text{C}$  and the temperature of last melting of ice from  $-3.7$  to  $-2.1$   $^{\circ}\text{C}$  (Supplemental Table 2). Using the software FLINCOR (Brown 1989) for the system  $\text{H}_2\text{O}-\text{NaCl}$  (their initial melting temperatures are similar to the eutectic temperature of the system  $\text{NaCl}-\text{H}_2\text{O}$ ), the corresponding salinities are 1.3 to 5.6 wt% NaCl equivalent (Supplemental Table 2, Fig. 5). The inclusions homogenize to

liquid between 190 and ~ 250 °C (Supplemental1 Table 2, Fig. 5). As the pressure corresponding to the interpreted depth of emplacement of the Serifos pluton is interpreted to have been 3 to 12 km (Seymour et al. 2009), the trapping temperature of the inclusions was estimated to be ~5 °C higher than the homogenization temperature (corrected by the FLINCOR software). To fully constrain the density and pressure of entrapment (hydrostatic) of the fluid we made use of the Package FLUIDS (Bakker 2012). The calculated hydrothermal trapping pressures for the L-V inclusions vary from 80 to 140 bars, and average 105 bars (s.d. = 10 bars). The fluid densities range from 0.84 to 0.90 g/mL.

### **Raman spectroscopy and gas chromatography**

Laser Raman and bulk composition chromatographic analyses were conducted on four L-V fluid inclusions hosted by stage I and IV clear quartz that had been analyzed microthermometrically (Supplemental1 Tables 3 and 4, Fig. 4b). Raman analyses reveal that the gaseous fluid phase is composed of H<sub>2</sub>O, CO<sub>2</sub>, O<sub>2</sub>, H<sub>2</sub>, and H<sub>2</sub>S. The logX<sub>CO<sub>2</sub>/H<sub>2</sub>O</sub>, logX<sub>O<sub>2</sub>/H<sub>2</sub>O</sub>, and logX<sub>H<sub>2</sub>S/H<sub>2</sub>O</sub> ratios range from of -1.0 to -0.8, -2.4 to -1.8, and -3.5 to -1.7, respectively. Also, to estimate temperature we have used the CO<sub>2</sub>- and CO<sub>2</sub>/H<sub>2</sub>S-geothermometers of Arnórsson and Gunnlaugsson (1985) and Nehring and D'Amore (1984). The calculated temperatures for stages I and IV are 235–248 and 190–197 °C, respectively.

Bulk analyses of the liquid phase showed that it contained the cations Na<sup>+</sup>, K<sup>+</sup>, Mg<sup>2+</sup>, Ca<sup>2+</sup>, Si<sup>4+</sup>, and the anions Cl<sup>-</sup>, SO<sub>4</sub><sup>2-</sup>, and HCO<sub>3</sub><sup>-</sup>. Si<sup>4+</sup> and HCO<sub>3</sub><sup>-</sup> are the dominant ions in

solution. These data allowed us to estimate the temperatures for the stages I and IV based on the Na-K-Ca geothermometer of Fournier and Truesdell (1973). The temperatures obtained were ~241 and 191–195 °C.

## **Isotope Geochemistry**

**Sulfur isotopes.** Sulfur isotope analyses were conducted on pyrite, sphalerite, chalcopyrite, greenockite, and galena (Table 2). The  $\delta^{34}\text{S}_{\text{V-CDT}}$  isotopic values of stage I pyrite, sphalerite, and chalcopyrite range from 2.7 to 5.1‰. Values of  $\delta^{34}\text{S}_{\text{V-CDT}}$  for stage II sphalerite and greenockite and III galena, were generally higher, i.e., 3.5, 5.5, and 5.0 to 5.6‰, respectively (Table 2). Temperatures of  $249 \pm 2$  °C and 226 °C were calculated for stage I and stage II from the pyrite-sphalerite and sphalerite-greenockite isotopic pairs, respectively, utilizing the equations of Ohmoto and Rye (1979), Ohmoto and Lasaga (1982), and Li and Liu (2006). The calculated  $\delta^{34}\text{S}_{\text{H}_2\text{S}}$  values of the mineralizing fluid range from 2.3 to 4.9‰ (stage I, pyrite, sphalerite, and chalcopyrite), 3.1 to 4.8‰ (stage II, sphalerite and greenockite), and 2.4 to 2.8‰ (stage III, galena) (Table 2). These  $\delta^{34}\text{S}_{\text{H}_2\text{S}}$  values reflect a dominantly magmatic source for sulfur for the ore fluids, i.e., the Serifos granodiorite.

**Lead isotopes.** Lead isotope data were obtained for stage I pyrite and stage III galena. Their  $^{206}\text{Pb}/^{204}\text{Pb}$  and  $^{207}\text{Pb}/^{204}\text{Pb}$  ratios range from 18.806 to  $18.902 \pm 0.001$  and 15.653 to  $15.702 \pm 0.001$  (Table 2). Our  $^{206}\text{Pb}/^{204}\text{Pb}$  and  $^{207}\text{Pb}/^{204}\text{Pb}$  values are very similar to those

obtained by Stos-Gale (1992) from the Serifos granodiorite (Kefala site, i.e., 18.882 to 18.870 and 15.636 to 15.699) (Fig. 6).

## Discussion

### Physicochemical Conditions of Native Bismuth Formation

Physicochemical conditions of Moutoulas mineralization were estimated from phase-stability relationships using SUPCRT92 (Johnson et al. 1992) with thermodynamic properties from the 2007 database (slop07.dat; Shock and Helgeson 1998). Reactions used to estimate these conditions and values of physicochemical parameters calculated using them are presented in Table 3. The corresponding phase relationships are illustrated graphically on pH vs.  $\log fO_2$  plots calculated for temperatures of 250 and 200 °C (Figs. 7a and 7b). These temperatures represent those estimated previously for stage I and stage IV, respectively (Supplemental1 Tables 2, 3, and 4; Table 2). All solids and gas species were considered behave ideally. Individual ion activity coefficients of dissolved species were calculated using the B- $\gamma$  extension of Helgeson et al. (1981) for an ionic strength (I) of 0.2.

The formation of sericite after orthoclase and albite in the inner alteration zone of the CBU schists require weakly acidic conditions during stage I (reactions 1 to 3, Table 3). A  $\log(\alpha_{K^+}/\alpha_{Na^+})$  value of 0.73, at 250 °C, was calculated based on the equilibrium between orthoclase and albite (reaction 3). The  $\log(\alpha_{K^+}/\alpha_{H^+})$  and  $\log(\alpha_{Na^+}/\alpha_{H^+})$  values obtained from reactions 1 and 2 are 3.7 and 2.4, and so the calculated  $\log \alpha_{Na^+}$  value is -0.47. The pH of the ore solution obtained from these values is 5.4.

A  $\log fS_2$  value of  $-13.8 \pm 0.2$  (PP-0.8, where PP is the pyrite-pyrrhotite buffer) was calculated for stage I from the pyrite and pyrrhotite equilibrium (reaction 4, Table 3). The maximum XFeS content of sphalerite coexisting with pyrite, for this stage is 25.8% and the calculated  $\log fS_2$  value is  $-14.1 \pm 0.2$  (PP-1.1) based on the equation of Barton and Skinner (1979). Using compositional data for the gas phase in the fluid inclusions (Supplemental Table 3; reaction 5 in Table 3) and the equations of McCartney and Lanyon (1989), we were also able to calculate the corresponding  $\log fO_2$  ( $-39.2$  or HM-2.1, where HM is the hematite-magnetite buffer) (Fig. 7a).

By stage IV, the temperature had decreased to  $200^\circ\text{C}$ ,  $\log fS_2$  decreased to  $-16.5 \pm 0.5$  (PP-1.4) and  $\log fO_2$  to  $-43.5$  (HM-3.5) (Fig. 7b). The value of  $\log fS_2$  was calculated from thermodynamic data for reaction 6, which describes the replacement of bismuthinite by native Bi, a common occurrence in late sub-stage IV. The value of  $\log fO_2$  was determined from compositional data for the gas phase in fluid inclusions as mentioned above for stage I (Table 3). The pH of the fluid (6.5) and the  $\log \alpha_{HS-(aq)}$  and  $\log \alpha_{H_2S(aq)}$  values ( $-2.9$  and  $-3.7$ ) were calculated using the equilibrium constants for reactions 7, 8, and 9 for the  $\log fO_2$  and  $\log fS_2$  values referred to above (Table 3). A value of  $\log fTe_2(g)$  ( $-17.0$ ) was calculated from a combination of reactions 10, 11, and 12. Increased  $\log fTe_2(g)$ ,  $\log \alpha_{H_2Te(aq)}$ , and  $\log \alpha_{HTe-(aq)}$  values is suggested to be responsible for the formation of tellurides (e.g., hessite and tetradyte) via reactions like 10 and 13 (Table 3).

During supergene alteration oxidation of native Bi (reaction 14) produced  $Bi(OH)^{2+}$  ions as the dominant dissolved species in solution. This reaction is promoted by higher  $\log fO_2$

values ( $-32.5$  or  $\text{HM}+10$ ) and a further decrease of pH of 7.1 (Table 3). The formation of bismutite  $[(\text{BiO}_2)_2\text{CO}_3]$  and bismite ( $\text{Bi}_2\text{O}_3$ ) was likely promoted by a reaction similar to 15 (Table 3).

#### Source of Metals Depositional Controls

Skarn formation, at Serifos, evolved from high-temperature magnetite ores to retrograde replacement and vein mineralization that culminated with the deposition of native bismuth. Figure 5 shows that the decrease in temperature from stage I ( $\sim 250^\circ\text{C}$ ) to stage IV ( $\sim 190^\circ\text{C}$ ) was accompanied by a roughly linear decrease in salinity from  $\sim 5.7$  to  $1.3$  wt% NaCl equivalent. This trend suggests dilution of the ore fluid as a result of mixing with waters of meteoric origin. Mixing of the ore fluid with oxidizing meteoric waters is also suggested by the gas chemistry, i.e., an increase of the  $\log \text{XO}_2/\text{H}_2\text{O}$  ratios from  $-3.4$ . The sulfur isotope data yielded a narrow range of calculated  $\delta^{34}\text{SH}_2\text{S}$  values, i.e., from  $2.3$  to  $4.9\text{‰}$  (Table 2). Such  $\delta^{34}\text{SH}_2\text{S}$  values reflect a dominantly magmatic source for the Bi-bearing mineralizing fluid. Further support is provided by the lead isotope data (Table 2) that suggest a mixed “Orogene” and “Upper Crust” source (Fig. 6). This implies that lead most probably derived from the Serifos pluton, which concurs with the lead data provided by Stos-Gale (1992). Pyrite, tetrahedrite-tennantite solid solutions, and galena from stages I, II, and III of the Moutoulas mineralization contain Bi, indicating that this element was incorporated during retrograde skarn formation and at early stages of the vein-type mineralization. This is consistent with the fact that the Serifos pluton appears relative enriched in Bi toward its margins (e.g., up to  $\sim 60\%$ , Seymour et al. 2009). The Serifos

skarn resembles the Lavrion (Greece), Stan Terg (Kosovo), and Wittichen Schwarzwald (Germany) Bi-bearing skarns. In these skarns, Bi is thought to be related to fluids derived from or equilibrated with a granodiorite during the retrograde skarn phase (Fig. 6, Voudouris et al. 2008a, 2008b; Kolodziejczyk et al. 2015; Staude et al. 2012).

The effects of temperature and pH on the solubility of  $\text{Bi}(\text{OH})^{2+}$  ions are summarized in a temperature vs. pH plot (Fig. 8). Calculation of the contours of the mass of  $\text{Bi}(\text{OH})^{2+}$  in solution was based on reaction 14 and the temperature, pH,  $\log f\text{O}_2$ ,  $\log f\text{S}_2$ , and  $\alpha\text{H}_2\text{S}$  values obtained for stages I and IV. Saturation of  $\text{Bi}(\text{OH})^{2+}$  is evident as the mass of  $\text{Bi}(\text{OH})^{2+}$  in solution decreases from  $T = 250$  to  $T = 200$  °C (Fig. 8). Here it is suggested that the conditions of stage I (lower pH and higher  $f\text{S}_2$  and  $f\text{O}_2$ ), favored the formation of Bi-enriched sulfides rather than the deposition of native bismuth. The proposed conditions for this stage lie within the stability fields of bismuthinite and pyrite, which show a broad overlap (Fig. 7a). At these conditions, as the ore solution was undersaturated in Bi (Fig. 8), the available Bi cannot form native bismuth and either is incorporated in the crystal lattice of the precipitated sulfides or forms submicroscopic grains within them (e.g., in pyrite and tetrahedrite, Supplemental Table 1).

During stage IV native bismuth formed via reaction 7 that was controlled by the interplay of six physicochemical parameters. Temperature decrease, pH neutralization,  $f\text{Te}_2$  increase coupled with decrease of  $f\text{S}_2$ ,  $\alpha\text{H}_2\text{S}$  ( $X_{\text{H}_2\text{S}}$  values decrease, Supplemental Table 3), and  $f\text{O}_2$  created a favorable environment for the precipitation of bismuthinite, then Bi-bearing tellurides, and native bismuth (Fig. 7b). At these more reducing and less acidic



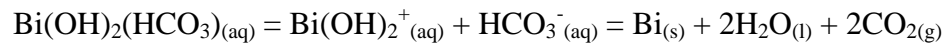
conditions the solubility of bismuth decreased (e.g., the  $\log \alpha_{\text{Bi}(\text{OH})^{2+}}$  values increased from  $-14.0$  to  $-11.2$ , Table 3, Fig. 8) thus leading to the precipitation of native bismuth.

We propose that variation of temperature, pH,  $\log f\text{S}_2$ ,  $\alpha\text{H}_2\text{S}$ ,  $\log f\text{O}_2$ , and  $\log f\text{Te}_2$  was related to fluid-rock interaction and subsequent dilution of the ore fluid (Fig. 6). At Moutoulas open hydrothermal system, interaction of the Bi-bearing fluid with the intensely fractured CBU marbles also led to the enrichment of the mineralizing fluid in  $\text{HCO}_3^-$  ions (Supplemental Table 4). Then supergene exposure and oxidation of the mineralization (e.g.,  $\text{HCO}_3^-$  (aq) anions required for reaction 15) may have resulted due to the intense exhumation and uplifting of the hydrothermal system (as it is suggested by Grasemann and Petrakakis 2007).

### Implications

Herein we examine native bismuth in the Serifos skarn and the conditions under which it may be precipitated. We suggest that proximity to a granodiorite, the development of magnetite ores and subsequent retrograde sulfide mineralization played important role in the precipitation of native bismuth, and we propose that in such a hydrothermal environment ( $\sim 200^\circ\text{C}$ ) there are six parameters, i.e., temperature, pH,  $\log f\text{S}_2$ ,  $\alpha\text{H}_2\text{S}$ ,  $\log f\text{O}_2$ , and  $\log f\text{Te}_2$  that control native bismuth precipitation. We find that wall-rock interaction and dilution of Bi-bearing magmatic fluids, i.e., containing  $\text{Bi}(\text{OH})^{2+}$  (aq), promoted native Bi saturation (Fig. 8) as these fluids facilitated a decrease in the mass of  $\text{Bi}(\text{OH})^{2+}$  ions in solution. We also propose that the formation of  $\text{Bi}(\text{OH})_x^{3-x}(\text{HCO}_3)_y^{3-y}$

complexes could play an important role on transporting this strategic element during wall-rock interaction. Destabilization of these complexes during dilution of the ore fluid via a probable reaction could be a mechanism controlling native bismuth precipitation:



**Acknowledgements:** We kindly thank Mr. Demosthenes Katsikis for his assistance with sampling in the Moutoulas mine. Critical comments from Dr. Mavrogenes are gratefully acknowledged.

## References

- Altherr, R., Kreuzer, H., Wendt, I., Lenz, H., Wagner, G.A., Keller, J., Harre, W., and Hohndorf, A. (1982), A late Oligocene/Early Miocene high temperature belt in the Attico-Cycladic crystalline complex (SE Pelagonia, Greece). *Geologisches Jahrbuch*, 23, 971-164.
- Afifi, A.M., Kelly, W.C., and Essene, E.J. (1988) Phase relations among tellurides, sulfides, and oxides: I. Thermochemical data and calculated equilibria. *Economic Geology*, 83, 377-294.
- Arnórsson, S., and Gunnlaugsson, E. (1985) New gas geothermometers for geothermal exploration-Calibration and application. *Geochimica and Cosmochimica Acta*, 49, 1307-1325.

- 361 Bakker, R.J. (2012) Package FLUIDS. Part 4: Thermodynamic modelling and purely empirical  
362 equations for H<sub>2</sub>O-NaCl-KCl solutions. *Mineralogy and Petrology*, 105, 1-29.
- 363 Barton, P.B.Jr, and Skinner, B.J. (1979) Sulfide mineral stabilities. In, Barnes, H.L., (Ed),  
364 Geochemistry of the hydrothermal ore deposits, 3<sup>rd</sup> Edition. Wiley, J., and Sons, New York,  
365 pp. 236-333.
- 366 Beaudoin, G., and Therrien, P. (2009) The updated web stable isotope fractionation calculator: In  
367 De Groot PA (ed), *Handbook of stable isotope analytical techniques*, Volume II, Elsevier,  
368 1120-1122.
- 369 Blundy, J.D., and Holland, T.J.B. (1990) Calcic amphibole equilibria and a new amphibole-  
370 plagioclase geothermometer. *Contributions to Mineralogy and Petrology*, 104, 208-224.
- 371 Bolhar, R., Ring, U., and Allen, C.M. (2010) An integrated zircon geochronological and  
372 geochemical investigation into the Miocene plutonic evolution of the Cyclades, Aegean Sea,  
373 Greece: Part 1: geochronology. *Contributions to Mineralogy and Petrology*, 160, 719-742.
- 374 Brichau, S., Thomson, S.N., and Ring, U. (2010) Thermochronometric constraints on the tectonic  
375 evolution of the Serifos detachment, Aegean Sea, Greece. *International Journal of Earth*  
376 *Sciences*, 99, 379-393, DOI 10.1007/s00531-008-0386-0.
- 377 Bröcker, M., and Franz, L. (2005) P-T conditions and timing of metamorphism at the base of the  
378 Cycladic Blueschist unit, Greece: The Panormos window on Tinos re-visited. *Neues*  
379 *Jahrbuch für Mineralogie Abhandlungen*, 181, 91-93.

- 380 Brown I.J., and Nesbitt B.E. (1987) Gold-copper-bismuth mineralization in hedenbergitic skarn.  
381 Tombstone Mountains, Yukon. Canadian Journal of Earth Sciences, 24, 2362-2372.
- 382 Brown, P.E. (1989) FLINCOR: A microcomputer program for the reduction and investigation of  
383 fluid inclusion data. American Mineralogist, 74, 1390-1393.
- 384 Chalkias, S., and Vavelidis, M. (1998) Interpretation of lead-isotope data from Greek Pb-Zn  
385 deposits, based on an empirical two-stage model. Bulletin of Geological Society of Greece,  
386 23,177-193.
- 387 Cook, N.J., Ciobanu, C.L., Spry, P.G., Voudouris, P., and the participants of the IGCP-486  
388 (2009) Understanding gold-(silver)-telluride-(selenide) mineral deposits. Episodes, 32, 249-  
389 263.
- 390 Dhamelincourt, P., Beny, J.M., Dubessy, J., and Poty, B. (1979) Analyse d' inclusions fluids à la  
391 microsonde mole à effet Raman. Bulletin Mineralogie, 102, 600-610.
- 392 Ducoux, M., Branquet, Y., Jolivet, L., Arbaret, L., Grasemann, B., Rabillard, A., Gumiaux, C.,  
393 Drufin, S. (2017) Synkinematic skarns and fluid drainage along detachments: The West  
394 Cycladic Detachment System on Serifos Island (Cyclades, Greece) and its related  
395 mineralization. Tectonophysics, 695, 1-26.
- 396 Etschmann, B.E., Liu, W., Pring, A., Grundler, P.V., Tooth, B., Borg, S., Testemale, D., Brewe,  
397 D., and Brugger, J. (2016) The role of Te (IV) and Bi(III) chloride complexes in

398 hydrothermal mass transfer: an X-ray absorption spectroscopic study. *Chemical Geology*,  
 399 425, 37-51.

400 Frezzotti, M.L., Tecce, F., and Casagli, A. (2012) Raman spectroscopy for fluid inclusion  
 401 analysis. *Journal of Geochemical Exploration*, 112, 1-20.

402 Fritz, P., Drimmie, R.J., and Norwick, K. (1974) Preparation of sulfur dioxide for mass  
 403 spectrometer analysis by combustion of sulfide with copper oxide. *Analytical Chemistry*, 76,  
 404 164-166.

405 Grasemann, B., and Petrakakis, K. (2007) Evolution of the Serifos metamorphic complex. In:  
 406 Lister, G., Forster, M., Ring, U. (Eds), *Inside the Aegean Metamorphic Core Complexes*.  
 407 *Journal of the Virtual Explorer*, 28, 1-18.

408 Grasemann, B., Schneider, D.A., Stockli, D.F., and Iglseder, C. (2012) Miocene bivergent crustal  
 409 extension in the Aegean: Evidence from the western Cyclades (Greece), *Lithosphere*, 4(1),  
 410 23–39, doi:10.1130/L164.1.

411 Henley, R.W., Mavrogenes, J.A., and Tanner, D. (2012) Sulfosalt melts and heavy metal (As-Sb-  
 412 Bi-Sn-Pb-Tl) fractionation during volcanic gas expansion: the El Indio (Chile) paleo-  
 413 fumarole. *Geofluids*, DOI: 10.1111/j.1468-8123.2011.00357.x.

414 Helgeson, H.C., Kirkham, D.H., and Flowers, G.C. (1981) Theoretical prediction of the  
 415 thermodynamic behavior of aqueous electrolytes at high pressures and temperatures,  
 416 Calculation of activity coefficients, osmotic coefficients, and apparent molal and standard

417 and relative partial molal properties to 600°C and 5kb. American Journal of Science, 281,  
418 1249-1516.

419 Johnson, J.W., Oelkers, E.H., and Helgeson, H.C. (1992) SUPCRT92, A software package for  
420 calculating the standard molal thermodynamic properties of minerals, gases, aqueous species  
421 and reactions from 1 to 5000 bars and 0° to 1000°C. Computer Geoscience, 18, 899-947.

422 Kołodziejczyk, J., Pršek, J., Melfos, V., Voudouris, P., Maliqi, F., and Kozub-Budzyń, G. (2015)  
423 Bismuth minerals from the Stan Terg deposit (Trepça, Kosovo). Mineralogical contribution  
424 to the evolution of the deposit. Neues Jahrbuch fur Mineralogie, 192, 317-333.

425 Li, Y., and Liu, J. (2006) Calculation of sulfur isotope fractionation in sulfides. Geochimica et  
426 Cosmochimica Acta, 70, 1789-1795.

427 Mavrogenes, J.A., Henley, R.W., Reyes, A.C., and Berger, B. (2010) Sulfosalt melts: evidence of  
428 high temperature vapor transport of metals in the formation of high sulfidation lode gold  
429 deposits. Economic Geology, 105, 257-262.

430 McCartney, R.A., and Lanyon, G.W. (1989) Calculations of steam fractions in vapor-dominated  
431 geothermal systems using an empirical method. In 14<sup>th</sup> Annual Workshop on Geothermal  
432 Reservoir Engineering, Stanford, p. 155-161.

433 Misra, K.C. (2000) Understanding mineral deposits. Kluwer Academic Publishers, Dordrecht,  
434 Netherlands.

- 435 Nehring, N.L., and D'Amore, F. (1984) Gas chemistry and thermometry of the Cerro Prieto,  
436 Mexico, geothermal field. *Geothermics*, 13, 75-89.
- 437 Ohmoto, H., and Lasaga, A.C. (1982) Kinetics of reactions between aqueous sulfates and sulfides  
438 in hydrothermal systems. *Geochimica et Cosmochimica Acta*, 46, 1727-1745.
- 439 Ohmoto, H., and Rye, R.O. (1979) Isotopes of sulfur and carbon. In: Barnes, H.L. (ed.)  
440 Geochemistry of the hydrothermal ore deposits, 3<sup>rd</sup> Edition, Wiley J and Sons, New York, p.  
441 509-567.
- 442 Pearce, J.A., Czernichowski-Lauriol, I., Lombardi, S., Brune, S., Nador, A., Baker, J., Pauwels,  
443 H., Hatziyannis, G., Beaubien, S., and Faber, E. (2004) A review of natural CO<sub>2</sub>  
444 accumulations in Europe as analogues for geological sequestration: Geological Society,  
445 London, Special Publication, 233, 29-41.
- 446 Petrakakis, K., Zamoyli, A., Iglseder, C., Rambousek, C., Grasemann, B., Dragamits, E., and  
447 Photiadis, A. (2007) Geological map of Serifos. 1:50.000. Geological map of Greece,  
448 Institute of Geological and Mineralogical Exploration, Athens, Greece.
- 449 Rabillard, A., Arbaret, L., Jolivet, L., Le Breton, N., Gumiaux, C., Augier, R., and Grasemann,  
450 B., (2015) A Interactions between plutonism and detachments during metamorphic core  
451 complex formation, Serifos Island (Cyclades, Greece). *Tectonics*, 34, 1080-1106, DOI:  
452 10.1002/2014TC003650.
- 453 Roedder, E. (1984) Fluid inclusions. *Reviews in Mineralogy*, 12, p. 550.

- 454 Salemink, J. (1985) Skarn and ore formation at Serifos, Greece as a consequence of granodiorite  
455 intrusion, 232 p. PhD thesis, Geology Ultraiectiona.
- 456 Seymour, K., Zouzias, D., Tombros, S.F., and Kolaiti, E. (2009). The geochemistry of the Serifos  
457 pluton and associated iron oxide and base metal sulphide ores: Skarn or metamorphosed  
458 exhalite deposits? Neues Jahrbuch für Mineralogie Abhandlungen, 186, 249-270, DOI:  
459 10.1127/0077-7757/2009/0143.
- 460 Shock, E.T., and Helgeson, H.C. (1998) Calculation of the thermodynamic and transport  
461 properties of aqueous species at high pressures and temperatures, Correlation algorithms for  
462 ionic species and equation of state prediction to 5 kb and 1000°C. Geochimica et  
463 Cosmochimica Acta, 52, 2009-2036.
- 464 Simon, G., and Essene, E.J. (1996) Phase relations among selenides, sulfides, tellurides, and  
465 oxides: I. Thermodynamic properties and calculated equilibria. Economic Geology, 91,  
466 1183-1208.
- 467 Skirrow, R.G., and Walshe J.L. (2002) Reduced and oxidized Au-Cu-Bi iron oxide deposits of  
468 the Tennant Creek Inlier, Australia: an integrated geologic model. Economic Geology, 97,  
469 1167-1202.
- 470 Schmidt, M.W. (1992) Amphibole composition in tonalite as a function of pressure: An  
471 experimental calibration of the Al-in-hornblende barometer. Contributions to Mineralogy  
472 and Petrology, 110, 304-310.



- 473 Staude, S., Werner, W., Mordhorst, T., Wemmer, K., Jacob, D.E., and Markl, G. (2012) Multi-  
474 stage Ag-Bi-Co-Ni-U and Cu-Bi vein mineralization at Wittichen, Schwarzwald, SW  
475 Germany: Geological setting, ore mineralogy, and fluid evolution. *Mineralium Deposita*, 47,  
476 251-276, DOI 10.1007/s00126-011-0365-4.
- 477 Stos-Gale, A.Z. (1992) Application of lead isotope analysis to provenance studies in archaeology.  
478 303 p. PhD thesis University of Oxford.
- 479 Stouraiti, C., and Mitropoulos, P. (1999) Variation in amphibole composition from the Serifos  
480 intrusive complex (Greece), under magmatic and hydrothermal alteration conditions. An  
481 application of hornblende geobarometry. *Bulletin of Geological Society of Greece*, 33, 39-  
482 50.
- 483 Tooth, B., Ciobanu, C.L., Green, L., O'Neill, B., and Brugger, J. (2011) Bi-melt formation and  
484 gold scavenging from hydrothermal fluids: an experimental study. *Geochimica et*  
485 *Cosmochimica Acta*, 75, 5423-5443.
- 486 Tooth, B., Brugger, J., Ciobanu, C., and Liu, W. (2008) Modeling of gold scavenging by bismuth  
487 melts coexisting with hydrothermal fluids. *Geology*, 36, 815-818.
- 488 Voudouris, P., Spry, P.G., Melfos, V., Alfieris, D., (2007). Tellurides and bismuth sulfosalts in  
489 gold occurrences of Greece: mineralogy and genetic considerations. *Geological Survey of*  
490 *Finland Guide* 53, 85-94.

- 491 Voudouris, P., Melfos, V., Spry, P.G., Bonsall, T., Tarkian, M., Economou-Eliopoulos, M.  
 492 (2008a) Mineralogy and fluid inclusion constraints on the evolution of the Plaka intrusion-  
 493 related ore system, Lavrion, Greece. *Mineralogy and Petrology*, 93, 79-110.
- 494 Voudouris, P., Melfos, V., Spry, P.G., Bonsall, T., Tarkian, M., Solomos, C. (2008b) Carbonate-  
 495 replacement Pb-Zn-Ag±Au mineralization in the Kamariza area, Lavrion, Greece:  
 496 Mineralogy and thermochemical conditions of formation. *Mineralogy and Petrology*, 94, 85-  
 497 106.
- 498 Xypolias, P., Iliopoulos, I., Chatzaras, V., and Kokkalas, S. (2012). Subduction and exhumation  
 499 related structures in the Cycladic Blueschists: insights from Evia Island (Aegean region,  
 500 Greece). *Tectonics*, 31, TC2001, doi: 10.1029/2011TC002946.
- 501 Yuan, H., Chen, K., Zhian, B., Zong, C., Dai, M., Fan, C., and Yin, C. (2013) Determination of  
 502 lead isotope compositions of geological samples using femtosecond laser ablation MC-  
 503 ICPMS. *Chinese Science Bulletin*, 58, 3914-3921.
- 504 Zartman, R.E., and Doe, B.R. (1981) Plumbotectonics. *The Model. Tectonophysics*, 75, 135-162.
- 505 Zhou, H., Sun, X., Fu, Y., Lin, H., and Jiang, L. (2016). Mineralogy and mineral chemistry of Bi-  
 506 minerals: Constraints on ore genesis of the Beiya giant porphyry-skarn gold deposit,  
 507 southwestern China. *Ore Geology Reviews* 79, 408-424.

508

## Figure Captions

Fig. 1. Simplified geological map of Serifos Island with the locations of magnetite exo- and endo-skarns, hematite ores, and sulfides (modified after Salemink 1985; Grasemann and Petrakakis 2007; Rabillard et al. 2015). The triangle represents the location of Figure 2.

Fig. 2. **(a)** A view of a sheared quartz vein at the interface between CBU schists and marbles containing the Bi-bearing assemblages studied. A bleached alteration halo is also evident. Also shown are the sampling sites **(b)** and **(c)**. **(b)** A hand specimen of the vein containing pyrite (Py) and galena (Gn) (scale bar = 1 cm). **(c)** Native bismuth (Bi) rimmed by a supergene assemblage (S) of beyerite, bismutite, and bismite (scale bar = 2 cm).

Fig. 3. Reflected light and backscattered electron images. **(a)** Stage I pyrite (Py) and sphalerite (Sp1) (scale bar = 1  $\mu$ m). **(b)** Stage I pyrite (Py) with pyrrhotite (Po) (reaction 4, Table 3, scale bar = 1 mm). **(c)** Stage II sphalerite (Sp2) and tetrahedrite-tennantite solid solutions (Tnt) filling fractures in brecciated stage I pyrite (Py) (scale bar = 1 mm). **(d)** Stage III galena (Gn) after stage I pyrite (Py) (scale bar = 100  $\mu$ m). **(e)** Late sub-stage IV native Bi (Bi) that replaced early sub-stage IV bismuthinite (Bst) (reaction 7, Table 3). Both minerals were partially oxidized to bismite (Bsm) (scale bar = 500  $\mu$ m). **(f)** Late sub-stage IV native Bi (Bi) after early sub-stage IV bismuthinite (Bst) and middle-sub-stage tetradyomite. Native Bi was oxidized to bismite (Bsm) (reactions 14 and 15, Table 3) (scale bar = 20  $\mu$ m).

Fig. 4. Photomicrographs of multiple fluid inclusion assemblages: **(a)** primary two-phase L-V (P) and secondary L-V (S) inclusions. The primary inclusions occur individually or as small,

randomly oriented clusters, whereas the secondary fluid inclusions form trails that are aligned along fractures and terminate at crystal growth surfaces (scale bar = 25  $\mu\text{m}$ ). **(b)** Detail of **a** showing the primary inclusions with low V-L ratios (vapor bubble occupies up to ~20 vol%) used for Raman spectroscopy (scale bar = 100  $\mu\text{m}$ ).

Fig. 5. Liquid-vapor trapping temperature vs. salinity plot in the system NaCl-H<sub>2</sub>O.

Fig. 6. A plot of  $^{206}\text{Pb}/^{204}\text{Pb}$  vs.  $^{207}\text{Pb}/^{204}\text{Pb}$  using age-corrected data. The galena crystals analyzed in this study plot between the “Orogene” and “Upper Crust” curves. The “Upper Crust,” “Orogene,” and “Mantle” were based on the model of Zartman and Doe (1981). Also shown are samples of galena from the Kefala pluton (Stos-Gale 1992) and the Moutoulas mineralization (Chalkias and Vavelidis 1998).

Fig. 7. (a)  $\log f\text{O}_2$  vs. pH plot for 250 °C, representing stage I of the Moutoulas skarn and vein mineralization. The dashed lines define the stability fields for pyrite (FeS<sub>2</sub>), pyrrhotite (FeS), hematite (Fe<sub>2</sub>O<sub>3</sub>), and magnetite (Fe<sub>3</sub>O<sub>4</sub>). The Fe-S-O mineral boundaries are shown for  $\Sigma\text{S} = 0.1$  mol/kg H<sub>2</sub>O. Also shown are the sulfur species in the system H-S-O (dotted lines), the stability boundary for muscovite-K-feldspar (short-dash-dotted line), and the stability fields for bismuthinite, maldonite (Au<sub>2</sub>Bi), and native bismuth (thick solid lines) fields. (b)  $\log f\text{O}_2$  vs. pH plot for 200 °C, representing stage IV of the Moutoulas skarn mineralization. The dashed lines define the stability fields for pyrite (FeS<sub>2</sub>), pyrrhotite (FeS), hematite (Fe<sub>2</sub>O<sub>3</sub>), and magnetite (Fe<sub>3</sub>O<sub>4</sub>). The Fe-S-O mineral boundaries are shown for  $\Sigma\text{S} = 0.1$  mol/kg H<sub>2</sub>O. The thin dotted and thin solid lines are the calculated contours for the sulfur and tellurium

species in solution. Also shown are the stability boundaries for kaolinite-sericite (short-dash-dotted line) and anglesite-galena (short-dotted lines) and the stability fields for the sulfur species in the system H-S-O (dotted lines), and bismuthinite-native bismuth (thick solid lines). Data from Barton and Skinner (1979), Simon and Essene (1996), Afifi et al. (1988), Skirrow and Walshe (2002), Tooth et al. (2008, 2011), and Staude et al. (2012) were employed to calculate the Bi mineral stability fields in the two diagrams.

Fig. 8. Temperature vs. pH plot summarizing changes in solubility of  $\text{Bi}(\text{OH})^{2+}$  ions (squares represent stage I and cycles stage IV). Calculation of the contours of mass in solution of  $\text{Bi}(\text{OH})^{2+}$  (in parts per million) was based on reaction 14, for  $\log \alpha_{\text{H}_2\text{S}} = -3.7$  and  $\log \alpha_{\Sigma\text{S}} = -3.0$ , and the  $\log f_{\text{O}_2}$  and  $\log f_{\text{S}_2}$  values obtained for stages I and IV. Also shown are the stability boundary bismuthinite and native bismuth (thick solid line).

**TABLE 1.** Ore paragenesis and vein fill minerals from Moutoulas area, Serifos

Mineral stages	Stage I	Stage II	Stage III	Stage IV <sup>a</sup>	Supergene stage
T (°C)	250			200	
Clear quartz	████████	████████	████████	████████	
Calcite			████████	████████	
Beyerite			■	████████	████████
Barite				████████	
Fluorite			████████	■	
Pyrite	████████				
Sphalerite	████████ <sup>a</sup>	■ <sup>b</sup>			
Chalcopyrite	████				
Arsenopyrite	■				
Pyrrhotite	■				
Tetrahedrite- tennantite and s.s.		████ <sup>c</sup>			
Greenockite		■			
Gersdorffite		■			
Galena			████████		
Bismuthinite <sup>e</sup>				■	
Tetradymite <sup>M</sup>				■	
Hessite <sup>M</sup>				■	
Melonite <sup>M</sup>				■	
Native bismuth <sup>L</sup>				████	████
Bismutite					████████
Bismite					████████
Covellite					████
Cerussite					████
Anglesite					████
Chalcocite					████
Goethite					████
Azurite					████
Malachite					████

Notes: Chemical formulas: bismuthinite ( $\text{Bi}_2\text{S}_3$ ), tetradymite ( $\text{Bi}_2\text{Te}_2\text{S}_3$ ), and melonite ( $\text{NiTe}_2$ ), beyerite [ $\text{Ca}(\text{BiO})_2(\text{CO}_3)_2$ ], bismutite [ $\text{Bi}_2\text{O}_2(\text{CO}_3)$ ], bismite ( $\text{Bi}_2\text{O}_3$ ). The boxes represent the abundance. <sup>a</sup> Stage IV composes of three sub-stages, i.e., <sup>E</sup> Early, <sup>M</sup> Middle, and <sup>L</sup> Late sub-stage.

<sup>a</sup>  $X_{\text{Fe5\%}} = 25.8$ , <sup>b</sup>  $X_{\text{Fe5\%}} = 13.8$ , <sup>c</sup>  $X_{\text{As}} = 1.9$  to 2.3.

**TABLE 2.** Sulfur and lead isotope data for pyrite, sphalerite, chalcopyrite, greenockite, and galena from the Moutoulas vein system, Serifos

Sample	Mineral	$\delta^{34}\text{S}$	$T^*$ (°C)	$\delta^{34}\text{S}_{\text{H}_2\text{S}}^b$	$^{206}\text{Pb}/^{204}\text{Pb}$	$^{207}\text{Pb}/^{204}\text{Pb}$
SE1	Pyrite (stage I) <sup>A</sup>	4.83	249	2.28	18.863	15.653
SE2	Pyrite (stage I) <sup>A</sup>	3.78	249	3.33	18.867	15.657
SE3	Pyrite (stage I)	4.44	249	2.94	18.871	15.661
SE4	Pyrite (stage I)	4.12	249	2.62	18.868	15.659
SE1	Sphalerite (stage I) <sup>A</sup>	3.73	249	3.33	—	—
SE2	Sphalerite (stage I) <sup>A</sup>	2.69	249	2.29	—	—
SE3	Sphalerite (stage II) <sup>B</sup>	3.54	226	3.14	—	—
SE2	Chalcopyrite (stage I)	5.08	249	4.88	—	—
SE3	Greenockite (stage II) <sup>B</sup>	5.49	226	4.79	—	—
SE1	Galena (stage III)	5.62	200	3.02	18.896	15.687
SE2	Galena (stage III)	5.04	200	2.44	18.902	15.694
SE3	Galena (stage III)	5.37	200	2.77	18.892	15.702

<sup>A</sup> Temperatures obtained from fluid inclusion data, the  $\text{CO}_2$ ,  $\text{CO}_2/\text{H}_2\text{S}$ , and Na-K-Ca geothermometers (Tables 3 and 4) and the pyrite-sphalerite (marked by <sup>A</sup>) and sphalerite-greenockite (marked by <sup>B</sup>) pairs; according to the equations of Ohmoto and Rye (1979), Ohmoto and Lasaga (1982), and Li and Liu (2006).

<sup>B</sup> Utilizing the  $\text{H}_2\text{S}$ -sulfide equations of Ohmoto and Rye (1979), Ohmoto and Lasaga (1982), and Li and Liu (2006).

**TABLE 3.** Reactions and corresponding values of selected physicochemical parameters applicable to the mineralizing fluid at Moutoulas, for temperatures of 250, 200, and 25 °C and an ionic strength  $I = 0.20$

	Reaction	$T$ (°C)	Calculated physicochemical parameters
1	$3\text{KAlSi}_3\text{O}_8(\text{s}) + 2\text{H}^+_{(\text{aq})} = \text{KAl}_3\text{Si}_3\text{O}_{10}(\text{OH})_{2(\text{s})} + 6\text{SiO}_{2(\text{aq})} + 2\text{K}^+_{(\text{aq})}$	250 <sup>A</sup>	$\log(\alpha_{\text{K}^+}/\alpha_{\text{H}^+}) = 3.7$ , pH = 5.4
2	$3\text{NaAlSi}_3\text{O}_8(\text{s}) + 2\text{H}^+_{(\text{aq})} + \text{K}^+_{(\text{aq})} = \text{KAl}_3\text{Si}_3\text{O}_{10}(\text{OH})_{2(\text{s})} + 6\text{SiO}_{2(\text{aq})} + 3\text{Na}^+_{(\text{aq})}$	250 <sup>A</sup>	$\log(\alpha_{\text{Na}^+}/\alpha_{\text{H}^+}) = 2.4$ , pH = 5.4
3	$\text{NaAlSi}_3\text{O}_8(\text{s}) + \text{K}^+_{(\text{aq})} = \text{KAlSi}_3\text{O}_8(\text{s}) + \text{Na}^+_{(\text{aq})}$	250 <sup>A</sup>	$\log(\alpha_{\text{K}^+}/\alpha_{\text{Na}^+}) = 0.73$ , pH = 5.4
4	$2\text{FeS}_{2(\text{s})} = 2\text{FeS}_{(\text{s})} + \text{S}_{2(\text{g})}$	250 <sup>A</sup>	$\log f_{\text{S}_{2(\text{g})}} = -13.8$
5	$2\text{H}_2\text{O}_{(\text{g})} = \text{O}_{2(\text{g})} + 2\text{H}_{2(\text{g})}$	250 <sup>A</sup> , 200 <sup>B</sup>	$\log f_{\text{O}_{2(\text{g})}} = -39.2$ and $-43.5$
6	$\text{Bi}_2\text{S}_{3(\text{s})} = 2\text{Bi}_{(\text{s})} + 1.5\text{S}_{2(\text{g})}$	200 <sup>B</sup>	pH = 6.5
7	$2\text{Bi}_2\text{S}_{3(\text{s})} + 6\text{H}_2\text{O}_{(\text{l})} = 4\text{Bi}_{(\text{s})} + 6\text{H}^+_{(\text{aq})} + 6\text{HS}^-_{(\text{aq})} + 6\text{O}_{2(\text{g})}$	200 <sup>B</sup>	$\log f_{\text{S}_{2(\text{g})}} = -16.5$
8	$\text{H}_2\text{S}_{(\text{aq})} = \text{H}^+_{(\text{aq})} + \text{HS}^-_{(\text{aq})}$	250, 200 <sup>B</sup>	$\log \alpha_{\text{HS}^-_{(\text{aq})}} = -1.8$ and $-2.9$
9	$2\text{H}_2\text{S}_{(\text{aq})} + \text{O}_{2(\text{g})} = \text{S}_{2(\text{g})} + 2\text{H}_2\text{O}_{(\text{l})}$	250, 200 <sup>B</sup>	$\log \alpha_{\text{HS}^-_{(\text{aq})}} = -1.8$ and $-2.9$
10	$\text{Ag}_2\text{Te}_{(\text{s})} + \text{H}_2\text{O}_{(\text{l})} = 2\text{Ag}_{(\text{s})} + \text{H}_2\text{Te}_{2(\text{aq})} + 0.5\text{O}_{2(\text{g})}$	200 <sup>B</sup>	$\log \alpha_{\text{H}_2\text{Te}_{2(\text{aq})}} = -5.2$
11	$2\text{H}_2\text{Te}_{(\text{aq})} + \text{O}_{2(\text{g})} = \text{Te}_{2(\text{g})} + 2\text{H}_2\text{O}_{(\text{l})}$	200 <sup>B</sup>	$\log f_{\text{Te}_{2(\text{g})}} = -17.0$
12	$\text{H}_2\text{Te}_{(\text{aq})} = \text{H}^+_{(\text{aq})} + \text{HTe}^-_{(\text{aq})}$	200 <sup>B</sup>	$\log \alpha_{\text{HTe}^-_{(\text{aq})}} = -3.8$
13	$2\text{Bi}(\text{OH})^{2+}_{(\text{aq})} + 2\text{H}_2\text{Te}_{(\text{aq})} + \text{H}_2\text{S}_{(\text{aq})} = \text{Bi}_{12}\text{Te}_2\text{S}_{(\text{s})} + 4\text{H}_2\text{O}_{(\text{l})} + 2\text{H}^+_{(\text{aq})}$	200 <sup>B</sup>	$\log \alpha_{\text{H}_2\text{S}_{(\text{aq})}} = -3.7$
14	$2\text{Bi}_{(\text{s})} + 1.5\text{O}_{2(\text{g})} + 4\text{H}^+_{(\text{aq})} = 2\text{Bi}(\text{OH})^{2+}_{(\text{aq})} + \text{H}_2\text{O}_{(\text{l})}$	250 <sup>A</sup> , 200 <sup>B</sup> , 25	$\log \alpha_{\text{Bi}(\text{OH})^{2+}_{(\text{aq})}} = -14.0$ , $-11.2$ , $-10.3$ , pH = 7.1
15	$4\text{Bi}(\text{OH})^{2+}_{(\text{aq})} + \text{HCO}^-_{3(\text{aq})} + \text{O}_{2(\text{g})} + \text{H}_2\text{O}_{2(\text{l})} = (\text{BiO}_2)_2\text{CO}_{3(\text{s})} + \text{Bi}_2\text{O}_{3(\text{s})}$	25	$\log f_{\text{O}_{2(\text{g})}} = -32.5$

Notes: <sup>A</sup> 250 and <sup>B</sup> 200 °C, temperatures based on fluid inclusions, the  $\text{CO}_2$ ,  $\text{CO}_2/\text{H}_2\text{S}$ , and Na-K-Ca-geothermometers, and pyrite-sphalerite and sphalerite-greenockite isotopic pairs (Tables 3, 4, and 5). The thermodynamic properties of bismuth complexes were compiled from Skirrow and Walshe (2002), Tooth et al. (2008, 2011), Staude et al. (2012), and Zhou et al. (2016). For reactions 5, 11, 12, 13, 14, and 15 the logK values are  $-5.2$ ,  $-4.7$ ,  $-1.1$ ,  $+11.7$ ,  $+6.9$ , and  $-12.6$ , respectively.

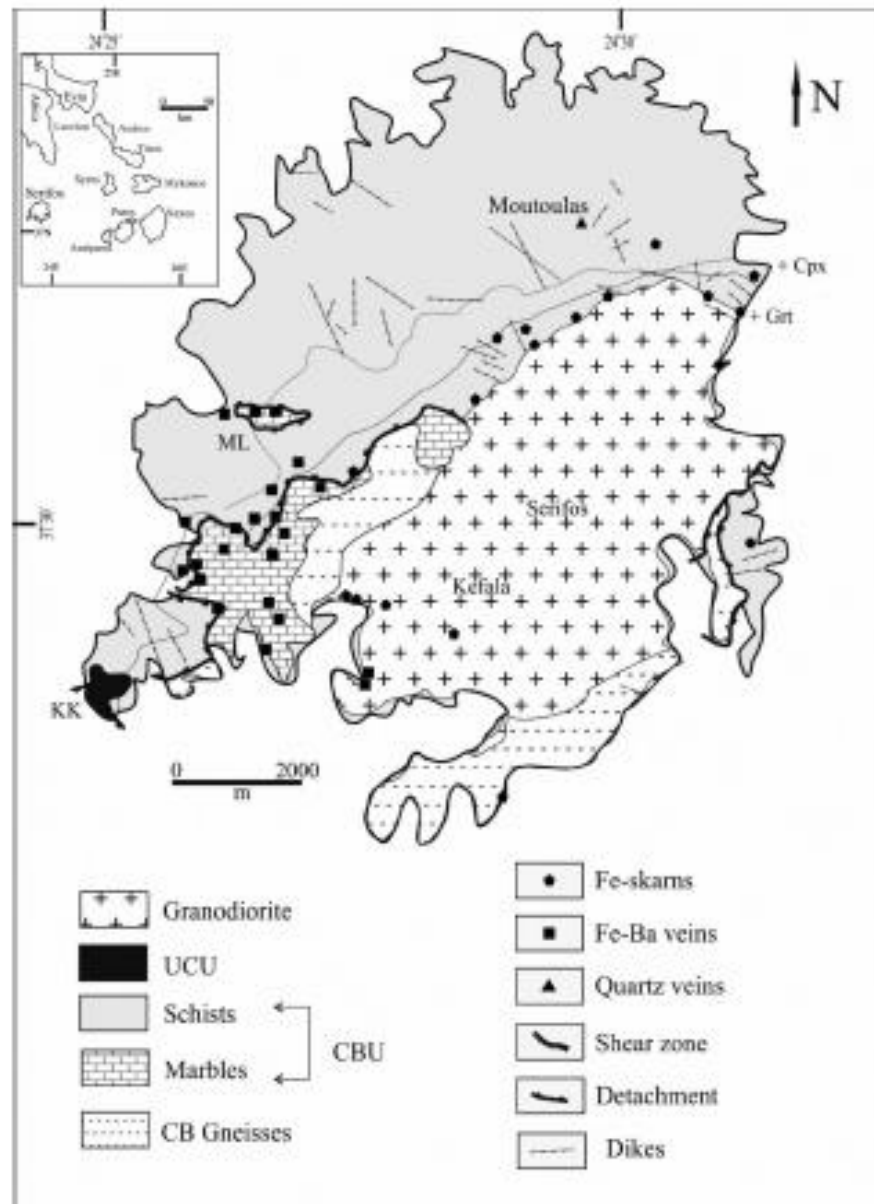


Fig. 1.



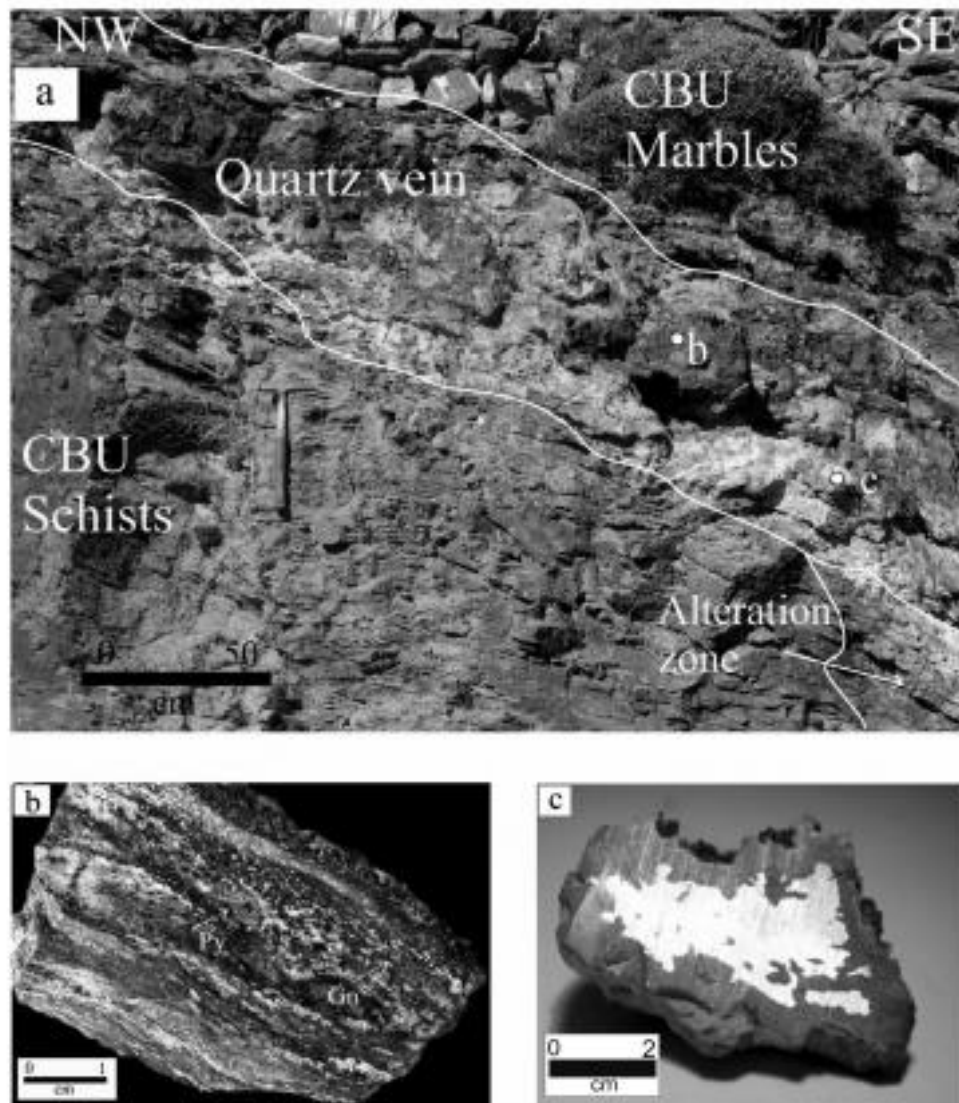


Fig. 2

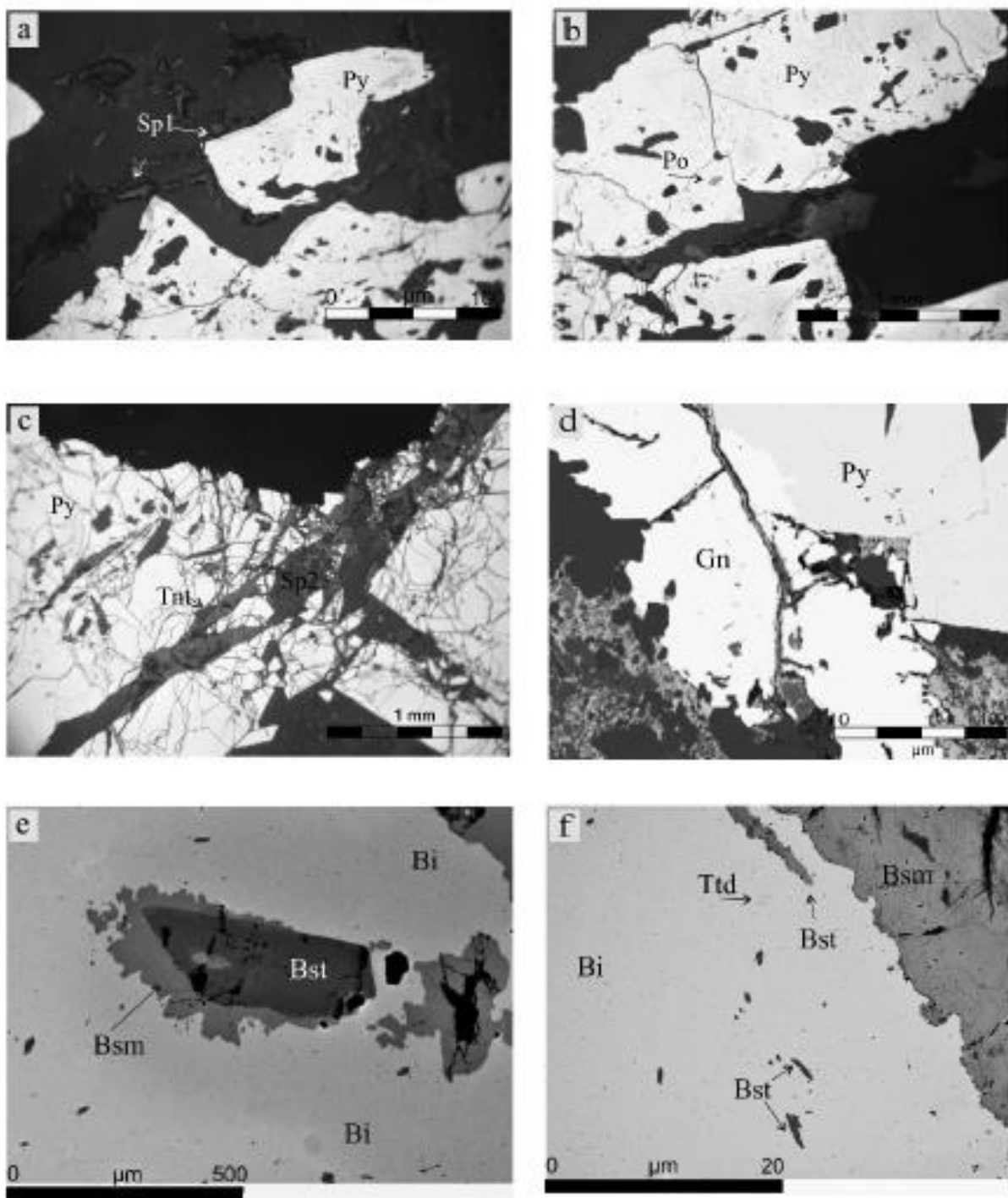


Fig. 3

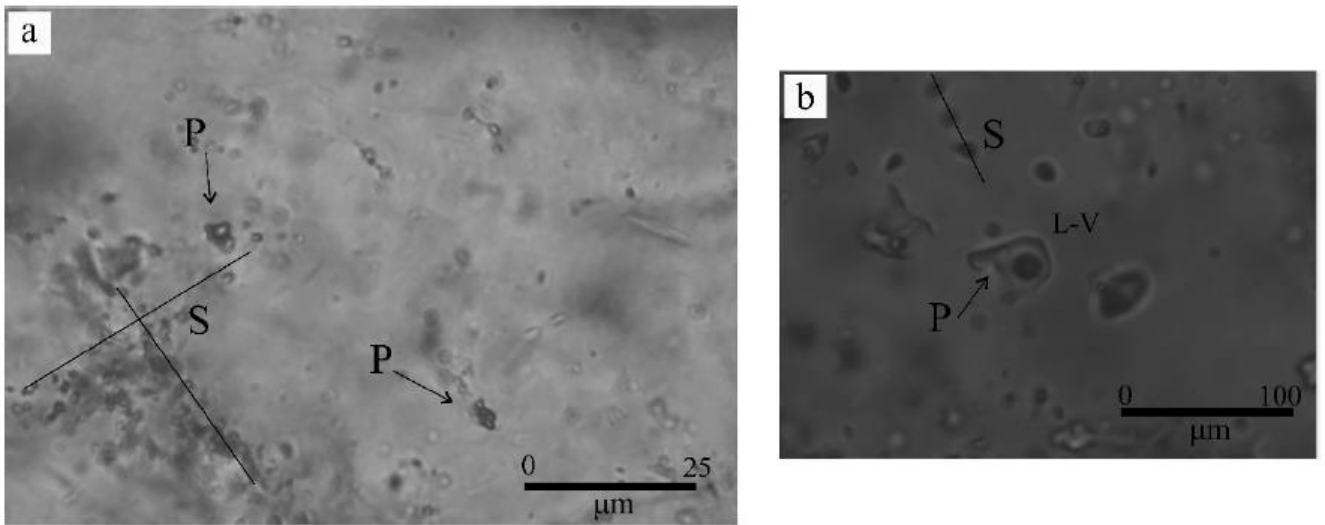


Fig. 4

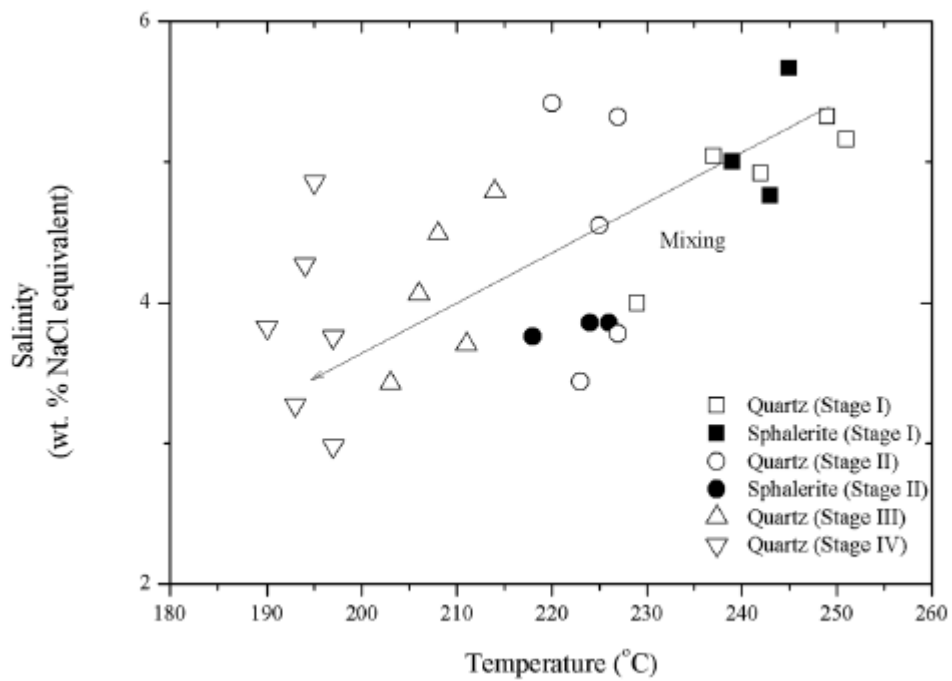


Fig. 5

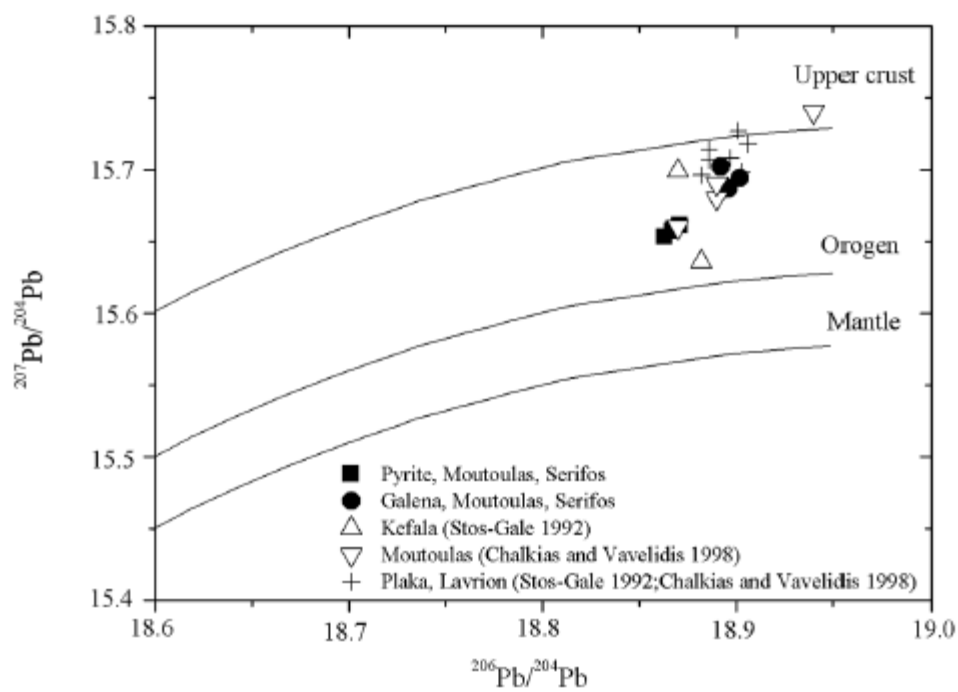


Fig. 6

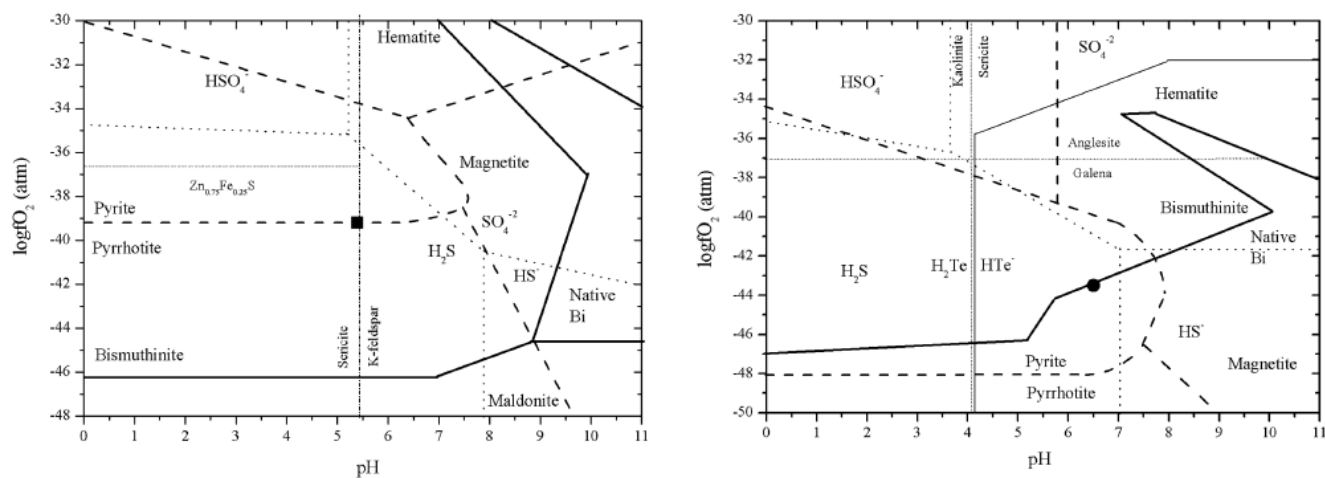


Fig. 7

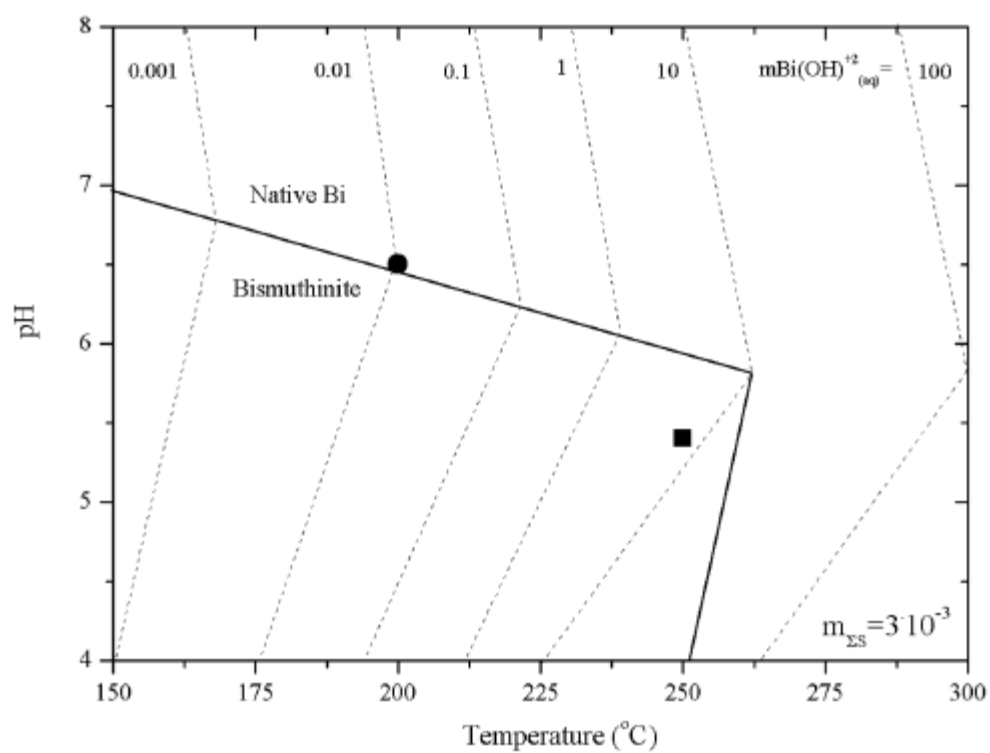


Fig. 8